

1 Retrieving Stratospheric Ozone Profiles from OMPS Limb

2 Profiler Measurements

3 Fang Zhu¹, Xiaoping Liu¹, Suwen Li¹, Fuqi Si²

4 ¹Anhui Province Key Laboratory of Pollutant Sensitive Materials and Environmental Remediation, Anhui Province Key
5 Laboratory of Intelligent Computing and Applications, School of Physics and Electrical Information, Huaibei Normal
6 University, Huaibei, 235000, Anhui, China

7 ²Centre of Environmental Optics, Anhui Institute of Optics and Fine Mechanics, Hefei Institutes of Physical Science,
8 Chinese Academy of Sciences, Hefei, Anhui 230031, China

9

10 Correspondence to: Fang Zhu (zhufang160@163.com)

11 **Abstract.** This study ~~presents an independent~~ retrieval algorithm combining wavelength pairing and the multiplicative
12 algebraic reconstruction technique (MART) to process Ozone Mapping and Profiler Suite (OMPS) limb observations for
13 vertical ozone profiles. ~~Developed as a complementary dataset for validating operational products, the algorithm is~~
14 ~~tailored to OMPS/LP's specific characteristics.~~ The retrieval algorithm employs scattered solar radiance measurements
15 from the OMPS limb profiler, focusing on the visible spectral range, normalizes this radiance to that at ~~an~~ upper tangent
16 height, and retrieves ozone concentrations between 12–40 km (~1 km vertical resolution). Additionally, it enables the
17 identification of cloud-contaminated measurements at specific altitudes within the ~~instrument~~ field of view. ~~A~~
18 ~~comprehensive error analysis reveals that prior uncertainty contributes ~5% error in the tropical lower stratosphere~~
19 ~~(based on a +5% perturbation experiment),~~ while a 30% uncertainty in the aerosol extinction coefficient causes ~5%
20 error at 15–25 km. ~~Absorption cross-section uncertainties introduce localized biases of -3% to -5%, and random~~
21 ~~measurement noise exhibits strong altitude dependence, with values below 10% in the mid-stratosphere and exceeding 20%~~
22 ~~at high altitudes and in the tropical upper troposphere.~~ OMPS data spanning the entire year of 2021 are processed, and
23 the results are evaluated through comparisons with multiple independent datasets, including NASA official products,
24 passive satellite observations, and in-situ measurements from balloon-borne ozonesondes. At 17–36 km, deviations from
25 OMPS/LP v2.6 data are ≤5%; at 18–35 km, consistency with Microwave Limb Sounder (MLS) v5.0 data ranges from 5–
26 10%; at 20–35 km, most deviations from OSIRIS v7.3 data are ≤5% (except near 23 km). Comparisons with ozonesonde
27 measurements reveal that differences in the 13–30 km range over northern mid-to-high latitudes are mostly <10% (with
28 10–15% differences at 22–25 km in polar regions). Over southern mid-latitudes, the consistency within the same altitude
29 range is 2–10%. Notably, deviations between the retrieved profiles and comparison products increase significantly in
30 low-altitude tropical regions.

删除的内容: describes a

删除的内容: the

删除的内容: instrument's

删除的内容: The retrieval error in the upper troposphere attributed to the prior profile is estimated to be 10-25%

31 1 Introduction

32 Stratospheric ozone forms a natural barrier protecting life on Earth by absorbing solar ultraviolet (UV) radiation.
33 Additionally, as a key greenhouse gas, it participates in the absorption and emission of infrared radiation in the
34 stratosphere, playing a crucial role in regulating Earth's energy balance and stabilizing the climate system (Li, ~~F.~~, et al.,
35 2023). Dynamic changes in stratospheric ozone concentrations not only directly reflect the emission fluxes and chemical
36 reaction processes of various atmospheric substances, but also serve as an important indicator for assessing the impact of
37 human activities on the atmospheric environment (Young et al., 2021; Chipperfield and Bekki, 2024). Since the

44 identification of the Antarctic ozone hole in the 1980s, research on the evolution patterns and driving mechanisms of
45 stratospheric ozone concentration has remained a core topic in atmospheric science, attracting global research efforts to
46 continuously explore its variation mechanisms and ecological effects.

47 High-precision retrieval of stratospheric ozone vertical profiles is a core requirement for advancing stratospheric
48 ozone research and establishing long-term essential climate variable datasets (Jia et al., 2015). To this end, multi-platform
49 monitoring technologies—including ground-based, balloon-borne, airborne, and satellite-based instruments—have been
50 widely applied over recent decades. Among these, satellite observations are categorized by detection modes into nadir,
51 occultation, and limb observations. Nadir-viewing instruments, which observe downward, offer excellent horizontal
52 coverage, with typical examples including the Ozone Monitoring Suite–Nadir (OMS-N) aboard Fengyun-3F
53 (NSMC,2025), the Ozone Monitoring Instrument (OMI) aboard Aura(Veefkind et al., 2006), and the Environmental
54 Monitoring Instrument (EMI) onboard the hyperspectral observation satellite GeoFen-5 (Qian et al., 2024). Occultation
55 instruments, which directly view the solar disk, are represented by the Stratospheric Aerosol and Gas Experiment (SAGE
56 III) (Cisewski et al., 2014), Atmospheric Chemistry Experiment (ACE) (Bernath et al., 2005), and Global Ozone
57 Monitoring by Occultation of Stars (GOMOS) (Bertaux et al., 2010), featuring high vertical resolution and good
58 signal-to-noise ratio. Limb scattering/emission observations combine the advantages of the aforementioned two modes,
59 boasting high sensitivity, favorable vertical resolution, and high spatial sampling rates, such as the Microwave Limb
60 Sounder (MLS) (Waters et al., 2006), SCanning Imaging Absorption spectroMeter for Atmospheric CartographY
61 (SCIAMACHY) (Burrows et al., 1995), and Optical Spectrograph and InfraRed Imager System (OSIRIS) (Llewellyn et
62 al., 2004). The Ozone Mapping and Profiler Suite (OMPS), a passive imaging spectrometer employed in this study, is
63 onboard the Suomi-National Polar-orbiting Partnership (SNPP) satellite (Flynn et al. 2014). Its limb profiler (OMPS/LP)
64 enables accurate retrieval of stratospheric ozone vertical profiles via limb observation mode. Since 2012, the NASA team
65 has successively developed and released four versions of the ozone LP retrieval algorithm for OMPS limb observation
66 data (the first version was released with operations (Rault et al,2013), the second version in 2014 (Xu et al.,2014),
67 version 2.5 in 2017 (DeLand et al., 2017), and version 2.6 in 2023_(Kramarova, 2023)). The University of Bremen has
68 also applied its self-developed retrieval algorithm to OMPS/LP measurements (Arosio et al., 2018). In addition, another
69 approach to processing OMPS/LP data employs a 2-D geometry retrieval method, as demonstrated in the work conducted
70 at the University of Saskatchewan (Zawada et al., 2018).

删除的内容: detect

删除的内容: strong signal strengths

删除的内容: Jaross et al., 2014

删除的内容: Flynn et al., 2014

71 This study focuses on ozone profile retrieval from OMPS/LP observation data, employing a retrieval algorithm
72 based on wavelength pairing and the multiplicative algebraic reconstruction technique (MART). The algorithm is derived
73 from the OSIRIS ozone profile retrieval scheme developed by the University of Saskatchewan. While the core retrieval
74 methodology of wavelength pairing and MART is well-established in limb sounding, the novelty of this work lies in its
75 tailored adaptation to the OMPS/LP instrument. Given the significant differences between OMPS/LP and OSIRIS in
76 measurement technologies—including spectral resolution, spectral channels, wavelength range, atmospheric sampling,
77 and radiance acquisition—this study has performed targeted optimizations and innovations on the algorithm. These
78 include significant adaptations in radiative transfer model construction, selection of retrieval spectra, and application of
79 atmospheric parameter databases. Furthermore, this study provides an independently developed retrieval pathway for
80 OMPS/LP, offering a complementary source for cross-validation with official products.

删除的内容: However,

删除的内容: given

81 The study aims to demonstrate the effectiveness of the wavelength pairing and MART algorithm for retrieving
82 OMPS/LP ozone profiles, thereby laying a theoretical and technical foundation for integrating OMPS/LP and OSIRIS
83 data to construct long-term continuous datasets. The structure of this paper is as follows: Section 2 details the
84 characteristics of the OMPS instrument, discussing its observational geometric principles and key issues in L1 data
85 calibration. Section 3 systematically elaborates on the retrieval algorithm, including its core framework, application
86 strategy of cloud filters, and parameter setting methods for the radiative transfer model. Section 4 conducts
87 multi-dimensional validation and statistical analysis of the retrievals, against NASA ozone profile products, MLS,

删除的内容: research

删除的内容: verify

删除的内容: in

删除的内容: in this study

删除的内容: combined with

99 OSIRIS, and ozonesonde datasets. Finally, the main results, key findings are summarized, and potential directions for
 100 future algorithm improvement are outlined in the conclusions.

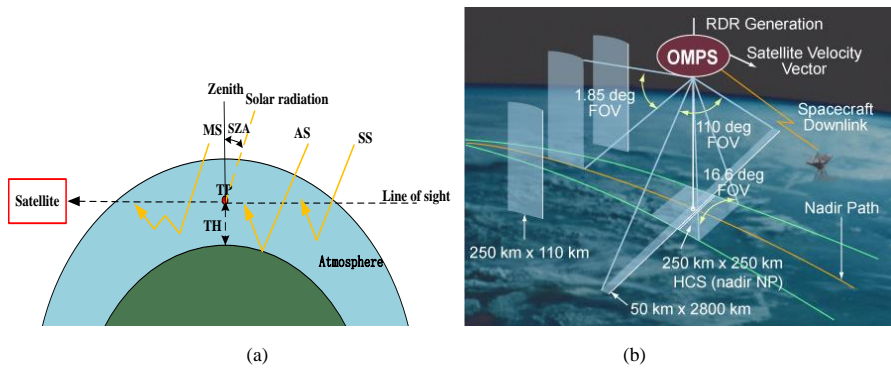
101 **2 OMPS/LP Ozone Retrieval**

102 **2.1 OMPS/LP instrument**

103 The OMPS instrument was successfully launched aboard the SNPP satellite on October 28, 2011 (Zhu et al., 2025).
 104 The satellite operates in a sun-synchronous polar orbit at an average altitude of 833 km with a 13:30 local time ascending
 105 node, commencing routine scientific observations in early 2012 (Kramarova et al., 2022). The OMPS suite integrates
 106 three distinct sensors: the Nadir Mapper (NM), Nadir Profiler (NP), and Limb Profiler (LP) (Flynn et al., 2014). Among
 107 them, OMPS/LP is centrally aimed at retrieving the vertical distribution of ozone in the Earth's middle atmosphere with
 108 high precision, employing a limb observation mode to sound the atmosphere by imaging the edge of the Earth's
 109 atmosphere. During a limb observation, the sensor's line-of-sight passes tangentially through the atmosphere, and the
 110 point along this path with the lowest altitude is termed the tangent point (TP). The vertical distance from this point to the
 111 Earth's geoid is referred to as the tangent height (TH). The fundamental geometry of this observation mode is depicted in
 112 Fig. 1a.

113 The spectral coverage of OMPS/LP ranges from 290 nm to 1000 nm, with spectral resolution varying with
 114 wavelength from 1.5 nm at short wavelengths to 40 nm at the longer-wavelengths. (Kramarova et al., 2014). Equipped
 115 with a charge-coupled device (CCD), the instrument can simultaneously observe scattered solar radiation across the full
 116 spectral range at altitudes from 0 to 100 km. Each detector pixel possesses an instantaneous vertical field of view of
 117 approximately 1.5 km. This configuration enables a high-precision vertical sampling of 1 km at the tangent point. (Jaross
 118 et al., 2014). To expand cross-track coverage, OMPS/LP is configured with three observation slits horizontally spaced by
 119 4.25° (approximately 250 km), whose observational geometry and field-of-view characteristics are illustrated in Fig. 1b.
 120 Each slit has a 1.85° vertical field of view (FOV), corresponding to a 110 km vertical observation range at the TP. This
 121 study focuses on measurement data from the central slit, which is aligned with the satellite's ground track. The SNPP
 122 satellite completes 14 orbits daily, with OMPS/LP performing approximately 160–180 measurements per orbit (at a
 123 latitudinal sampling interval of ~1°). LP can achieve global coverage every 3–4 days (Kramarova et al., 2024).

- 删除的内容: Arosio et al., 2018
- 删除的内容: scanning
- 删除的内容: intersects
- 删除的内容: the Earth's surface at a specific location, which is termed the tangent point (TP)
- 删除的内容: by wavelength—reaching 1.5 nm at the short-wavelength end and 40 nm at the longer-wavelength end
- 删除的内容: resolution
- 删除的内容: operates
- 删除的内容: completing



124
 125
 126 **Figure 1.** (a) Schematic of the satellite limb observation geometry, indicating the key parameters of tangent point (TP) and tangent
 127 height (TH) (SS: single scattering, AS: albedo scattering, MS: multiple scattering, SZA: solar zenith angle) (adapted from Arosio et al.,
 128 2018); (b) Schematic diagram of OMPS observation geometry and field-of-view characteristics (Kramarova et al., 2018).

142 **2.2 Key corrections in OMPS/LP L1G v2.6 data,**

删除的内容: OMPS LP L1 calibration

143 Radiometric errors and sensor pointing errors are the two main error sources affecting limb-scattering ozone
144 retrieval accuracy (Kramarova et al., 2024). The OMPS/LP L1G v2.6 dataset incorporates essential corrections to
145 address these issues.

删除的内容: (primarily involving altitude registration errors)

146 Pointing (altitude registration) corrections are applied to mitigate tangent height offsets caused by instrument
147 alignment and thermal effects. Multi-point corrections include static, intra-orbit, and time-dependent adjustments
148 following Moy et al. (2017).

删除的内容: the accuracy of ozone profile retrieval via limb scattering techniques

149 Stray light correction is performed using an updated point spread function (PSF) based on pre-launch
150 measurements (Jaross et al., 2014). In version 2.6, the PSF tail intensity in UV and VIS/NIR bands is increased by
151 ~12% to improve high-altitude stray light estimation (Kramarova et al., 2024). An additional factor of 1.5 is applied
152 in VIS/NIR wavelengths to correct for in-band scattering. While thermally induced wavelength shifts have
153 negligible impact on height-normalized radiances in ozone retrieval, we note that residual wavelength-dependent
154 errors could affect cross-section matching in regions of strong ozone absorption.

删除的内容: In this section, we describe the instrument calibration in OMPS/LP L1G v2.6 processing.

155 These calibration steps are critical for ensuring the radiometric and geometric accuracy of the radiances used
156 in our retrieval. Further details can be found in the cited references.

删除的内容: Sensor pointing information is primarily acquired via the dual star trackers in the SNPP spacecraft's attitude determination system. However, misalignment between the attitude control frame and the fuselage frame, as well as thermally induced deformation of LP optical components, can lead to significant pointing offsets. To address this, multi-point corrections are implemented in L1G data processing following the method by Moy et al. (2017). The v2.6 version employs three types of corrections: static, intra-orbit, and time-dependent. The static correction for the central slit is 1.58 km. Intra-orbit corrections are based on the absolute radiometric residual method (ARRM) with linear adjustments along the south-north direction of the orbit; time-dependent corrections apply a uniform offset of +0.1 km. .

157 **3 Retrieval method**

158 **3.1 Retrieval vector**

159 The retrieval method for vertical ozone concentration distributions based on OMPS/LP measurements in this study
160 draws on the technical framework developed by Zhu et al.(2021), who derived ozone number density profiles using
161 SCIAMACHY limb scattering measurements in the Chappuis–Wulf band. It shares similar methodological principles
162 with the approaches proposed by Roth et al. (2007) and Degenstein et al. (2009), all of which employ retrieval vectors
163 positively correlated with ozone concentrations for calculations.

164 The first step in the retrieval process involves normalizing the limb radiance at selected wavelengths. This
165 operation entails normalizing the limb radiance at each wavelength to a reference TH, which effectively eliminates
166 interference from the solar Fraunhofer structure, weakens the impact of surface reflection, and simultaneously achieves
167 instrument self-calibration (Jia et al., 2015).

168
$$I_{\text{nor}}(\lambda, H) = I(\lambda, H) / I(\lambda, H_{\text{ref}}) \tag{1}$$

169 where, H denotes the TH, and λ represents the wavelength. $I(\lambda, H_{\text{ref}})$ and $I_{\text{nor}}(\lambda, H)$ refer to the radiance at the
170 reference TH and the normalized radiance, respectively. The reference TH is an upper altitude where ozone sensitivity is
171 low; in this study, it is selected as 40.5 km (i.e., the reference TH above the maximum retrieval altitude). Although
172 radiance normalization cannot completely eliminate the influence of surface reflection or correct spectral errors such as
173 wavelength shifts (which affect the calculation of ozone absorption cross-sections), it significantly reduces the
174 requirements for both absolute radiometric calibration and modeling accuracy (Flittner et al., 2000). To mitigate the
175 effect of aerosol scattering, the Chappuis triplet vector (CTV) method proposed by Degenstein et al. (2009) and Flittner
176 et al. (2000) is employed for wavelength pairing. In the Chappuis-Wulf band, the CTV is defined as the difference
177 between the logarithmic average of normalized radiances at two weakly ozone-absorbing wavelengths and the logarithm
178 of the normalized radiance at a wavelength near the ozone absorption peak, thereby isolating the ozone absorption signal

删除的内容: Two-dimensional CCD detectors are susceptible to interference from internally scattered stray light, causing photons from intense light regions in the scene to scatter into weak signal areas. Jaross et al. (2014) proposed a stray light (SL) correction scheme based on pre-launch point spread function (PSF)

275 | from common background scattering effects (e.g., aerosol scattering). It is expressed as:

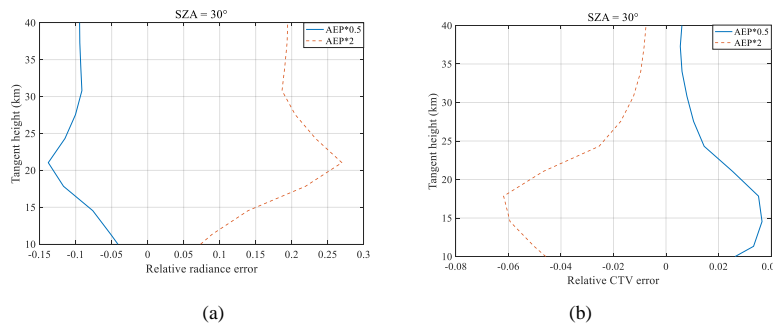
$$276 \quad y_j = \ln \left(\frac{I_{\text{nor}}(\lambda_{\text{ref}1,j}) I_{\text{nor}}(\lambda_{\text{ref}2,j})}{I_{\text{nor}}(\lambda_p,j)} \right) \quad (2)$$

277 where, j denotes the index of the TH measured by the instrument, and y_j represents the retrieval vector after
 278 wavelength pairing at the j^{th} of TH. $\lambda_{\text{ref}1}$, $\lambda_{\text{ref}2}$, and λ_p correspond to the weakly ozone-absorbing reference
 279 wavelengths and the strongly absorbing peak wavelength, respectively. In this study, the peak wavelength $\lambda_p=606.3$ nm
 280 adheres to the visible channel configuration employed in the NASA OMPS/LP v2.6 operational algorithm (Kramarova, et
 281 al., 2024), thereby consistency with established OMPS retrieval products. The weakly absorbing reference wavelengths
 282 $\lambda_{\text{ref}1}=512$ nm and $\lambda_{\text{ref}2}=675.5$ nm were optimized according to the selection criteria proposed by Zhu et al. (2021) for
 283 limb scattering ozone retrievals within the Chappuis-Wulf band, which take into account the specific spectral response
 284 and noise characteristics of OMPS/LP. Unlike the NASA algorithm, which uses spectral averages over multiple
 285 wavelengths for its visible triplet (510 nm, 606 nm, 675 nm; Kramarova and DeLand, 2023), the proposed method adopts
 286 individual discrete wavelength channels.

287 The paired measurement vectors maintain high sensitivity to ozone concentration. The CTV is designed to be
 288 positively correlated with ozone concentration (Degenstein et al., 2009). As expected, the CTV values and the retrieved
 289 ozone profiles show consistent vertical and latitudinal variations, with peak altitudes decreasing from the tropics to high
 290 latitudes. In this study, CTV values near zero above 35 km exhibit insufficient sensitivity to ozone, and values above
 291 40 km become negative; therefore, the retrieval is restricted to altitudes below 40 km.

292 Aerosols, as suspended particles capable of absorbing and scattering light, have sources including both natural and
 293 anthropogenic factors. Stratospheric aerosols mainly originate from SO₂, HCl released by volcanic eruptions, naturally
 294 generated OCS, and pollutants such as SO₂ from industrial emissions (Li, Z., et al., 2023). The presence of aerosols
 295 enhances the intensity of atmospheric scattered light, with the effect being stronger at longer (red) wavelengths than at
 296 shorter (blue) wavelengths due to wavelength-dependent scattering. Based on the SCIATRAN model (radiative
 297 TRANsfer model for SCIAMACHY), this study conducted simulation experiments on aerosol extinction coefficients to
 298 explore their impacts on radiance and CTV.

299 Fig. 2 shows the effects of aerosol extinction profiles with different scaling factors on radiance and CTV. When the
 300 aerosol profile varies within the range of 0.1-10 times the standard value, the radiance profile is positively correlated with
 301 the aerosol extinction coefficient, while CTV decreases as the extinction coefficient increases, with the impact mainly
 302 concentrated below 30 km. For instance, when the aerosol extinction profile doubles, the radiance at 21 km increases by
 303 27%, whereas the CTV decreases by only 5%. It indicates that wavelength pairing can weaken the aerosol scattering
 304 effect but cannot completely eliminate it. In addition, the study found that both radiance errors and CTV errors increase
 305 with an increase in SZA.

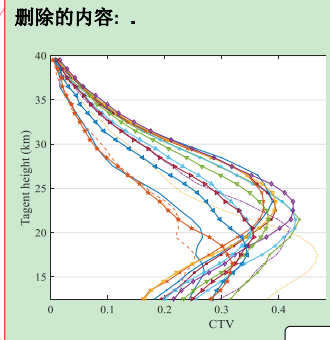


306 **Figure 2.** Variations in radiance and CTV with aerosol extinction coefficients of different multiples. (a) Relative radiance error; (b)
 307 Relative CTV error.

删除的内容: thereby enhancing the specificity of the retrieval signal.

删除的内容: referencing the wavelength system by Kramarova et al. (2024) and the selection criteria by Zhu et al. (2021), $\lambda_{\text{ref}1}$ is set to 512 nm, $\lambda_{\text{ref}2}$ to 606.3 nm, and λ_p to 675.5 nm.

带格式的: 缩进: 首行缩进: 2 字符



带格式的: 字体: (默认) Times New Roman, 小四

删除的内容: The CTVs and retrieved ozone profiles across

带格式的: 字体: (默认) Times New Roman, 小四

删除的内容: relative increment of red waves in the spectrum being higher

删除的内容: 3

删除的内容: multiples

删除的内容: 40

删除的内容: value

删除的内容: while

删除的内容:

删除的内容: 3

带格式的: 字体: 小五

带格式的: 缩进: 首行缩进: 0 字符

375 3.2 Multiplicative algebraic relaxation technology

376 Given the nonlinear nature of the retrieval problem, this study employs an iterative method for solution and selects
377 the multiplicative algebraic reconstruction technique (MART) to perform ozone profile retrieval. As an improved
378 algorithm of nonlinear relaxation techniques, MART has a main advantage in that it can utilize multiple sets of
379 measurement vectors to realize the retrieval of atmospheric state parameters at any altitude (Roth et al., 2007). During the
380 iteration process, the update of atmospheric states at each altitude depends on a multiplicative factor, which is obtained
381 by weighted averaging the ratios of all valid observation vectors to simulation vectors. The general formula of the MART
382 algorithm is as follows:

$$383 x_i^{(n+1)} = x_i^{(n)} \sum_j \left(\frac{y_j^{\text{obs}}}{y_j^{\text{mod}}} W_{ji} \right) \quad (3)$$

384 where, $x_i^{(n)}$ denotes the ozone number density at atmospheric height i during the n^{th} iteration; y_j^{obs} and y_j^{mod}
385 represent the observation vector and simulation vector processed via Equations (1) and (2), respectively, where y^{mod} is
386 generated by the radiative transfer model based on the ozone profile $x^{(n)}$ obtained from the n^{th} iteration; W_{ji} is the
387 line-of-sight weight factor, indicating the importance of the j^{th} TH or line of sight to the ozone retrieved at altitude, i . At
388 each altitude, $\sum_j W_{ji} = 1$. The value of W_{ji} in this study follows the setting in Zhu et al., (2021).

删除的内容: influence weight

删除的内容: on atmospheric height

389 3.3 Cloud filter

390 A critical step in the OMPS/LP ozone profile retrieval is to define the lower boundary by determining cloud top
391 height. This is accomplished using a cloud detection method, modified from Chen et al. (2016), which leverages the
392 spectral contrast in radiance between red and near-infrared bands. The method quantifies this contrast by computing the
393 change in the vertical radiance gradient between two selected wavelengths. The underlying premise of the gradient-based
394 cloud detection algorithm is that clouds generate a significantly larger radiance gradient compared to aerosols. This
395 gradient is quantitatively defined as the rate of change of radiance with respect to TH:

$$396 G(\lambda, H) = \partial \ln I(\lambda, H) / \partial H \quad (4)$$

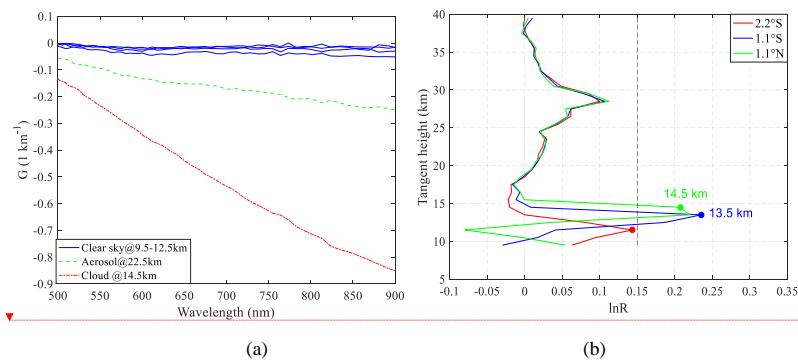
397 As shown in Fig. 3a, the variation characteristics of radiance gradient with wavelength in the 500-900 nm provide a
398 basis for determining cloud top height. In cloud-free conditions, the radiance intensity varies slightly with wavelength;
399 whereas in the presence of clouds, the wavelength dependence of radiance is significantly stronger than that of aerosols.
400 Based on this, in this study, the cloud top height is determined by calculating the spectral gradient difference, with the
401 formula as follows:

$$402 \ln R(H) = [G(\lambda_s, H) - G(\lambda_l, H)] \quad (5)$$

403 where, λ_s and λ_l denote the short wavelength and long wavelength, respectively. In this study, λ_s is set to 674 nm, and
404 λ_l is set to 868 nm. The positive cloud detection threshold for LP data is 1.5, which is also applicable to the detection of
405 polar mesospheric clouds (PMCs). Taking the SNPP satellite orbit 51220 on September 15, 2021 as an example (Fig. 3b),
406 the characteristics of $\ln R$ profiles differ significantly between two cloudy events and one cloud-free event: the
407 maximum value of $\ln R$ in the cloud-free event is below 1.5, while that in the cloudy events is above this threshold, and
408 the TH corresponding to the maximum $\ln R$ value is the cloud top height. During the ozone retrieval process, retrieval
409 below the cloud top height is not performed, and the profile in this region remains unchanged.

删除的内容: 4a

删除的内容: 4b



删除的内容: the multiplication factor of the ozone profile below the cloud top height remains unchanged. .
带格式的: 居中

414
415
416
417
418
419

Figure 3. Radiance gradient $G(\lambda, H)$ and gradient difference $\ln R$ during orbit 51220 on September 15, 2021. (a) Radiance gradient $G(\lambda, H)$ spectrum at 3°N under different atmospheric conditions: clear sky (blue), cloud (red), and aerosol (green); (b) Radiance gradient difference $\ln R$ derived from OMPS/LP measurements for three equatorial events, showing the cloud detection results. The black dashed line represents the threshold employed for cloud identification.

删除的内容: 4

420 **3.4 Implementation details**

421 In this study, the SCIATRAN v2.2 toolbox (Roazanov et al., 2017) is employed as the forward modeling to calculate
422 the simulated radiances required for ozone concentration retrieval. The observed and simulated radiances are processed
423 through normalization and wavelength pairing to form retrieval vectors, which serve as inputs to the MART algorithm to
424 drive the iterative update of ozone profiles.

425 The radiative transfer solution in the forward model is based on the discrete ordinate method applied to a spherical
426 atmosphere with a pseudo-spherical approximation for multiple scattering. The solution incorporates the effects of
427 multiple scattering and refraction while explicitly omitting polarization. Radiance calculations in the model are focused
428 solely on ozone, an absorbing gas, with the ozone absorption cross-sections referenced from the research results of
429 Bogumil et al. (2000). The pressure and temperature profiles used in this study were obtained from the Global Modeling
430 and Assimilation Office (GMAO) interpolated dataset. These meteorological data are incorporated in the OMPS/LP L1G
431 dataset provided by NASA (NASA, 2025a). In addition, the model sets the stratospheric background aerosol type as
432 LOWTRAN (Kneizys, 1988), the boundary layer humidity as 80%, and the boundary layer aerosol type as marine. The
433 retrieved ozone profiles are reported on the same vertical grid as the OMPS/LP L1G input data, which has a fixed
434 spacing of 1 km in tangent height. However, this sampling interval does not imply an equivalent effective vertical
435 resolution. The true vertical resolution is generally coarser than 1 km, particularly in regions of lower measurement
436 sensitivity. The prior profiles are from SCIATRAN's built-in database. These profiles are provided by McLinden
437 climatology (C. McLinden, Meteorological Service of Canada, personal communication) and include monthly and
438 latitude-dependent vertical distributions of volume mixing ratios for O_3 , NO_2 , BrO , and OCIO , as well as pressure and
439 temperature in the 0 to 100 km altitude range. The volume mixing ratio of ozone can be converted to ozone number
440 density based on temperature and pressure.

删除的内容: 1986
删除的内容: vertical resolution of the
删除的内容: retrieval is fundamentally constrained by the native resolution of the input data. Given that
删除的内容: data are provided on a fixed 1 km TH grid, the resulting profiles consequently exhibit a vertical resolution of 1 km

441 **4 Results**

442 This section presents the processing results derived from the full year of 2021 OMPS-LP data. We utilized the L1G
443 v2.6 dataset (Jaross, 2023), which incorporates enhanced stray light correction and pointing accuracy as detailed in

458 Section 2.2. The analysis is based exclusively on measurements from the instrument's central slit.

459 4.1 Error analysis

460 In the field of error analysis, on limb-scattering ozone retrieval, there is a wealth of academic achievements. Zhu et
461 al. (2022) used numerical perturbation, to conduct formal error analysis on the retrieval method of the weighted
462 multiplicative algebraic reconstruction technique, accurately quantifying ozone retrieval errors at different altitudes.
463 Arosio et al. (2022) systematically evaluated random errors and systematic errors for stratospheric ozone profile retrieval
464 based on optimal estimation (OE) algorithms (Rodgers, 2000). These research results provide important references for
465 the error analysis of MART retrieval algorithm, and the error estimation results of this study are consistent with those in
466 Arosio et al. (2022) and Zhu et al. (2022).

467 To ensure data quality, radiance measurements contaminated by clouds were systematically excluded during
468 retrieval. Furthermore, the scene reflectance was determined directly from OMPS/LP radiance measurements at 675 nm,
469 and the corrected THs provided in the NASA L1G data were adopted. Accordingly, the retrieval error budget focuses on
470 four primary sources: prior profiles, aerosols extinction profile, ozone absorption cross-sections, and measurement noise.

471 The sensitivity of retrieval to the true state and the contribution of prior information can be formally described
472 through the averaging kernel and measurement response (Rodgers, 2000; von Clarmann et al., 2020). However, unlike
473 OE approaches, the MART algorithm used in this study does not produce formal averaging kernels. Therefore, we assess
474 the sensitivity of the retrieval to the prior profile through a perturbation-based approach. In this study, the prior sensitivity
475 analysis matrix A_0 is used to quantify the sensitivity of retrieval to the prior profile, and its expression is as follows:

$$476 A_0 = \frac{\partial \hat{x}}{\partial x_0} \quad (6)$$

477 where x_0 and \hat{x} represent the initial ozone profile and the retrieved ozone profile, respectively. To calculate the column
478 vectors of A_0 , the ozone concentration at a single altitude was perturbed in x_0 by 5% and analyzes the corresponding
479 changes in \hat{x} . A_0 is a dimensionless matrix, whose characteristics can intuitively reflect the impact of changes in the
480 prior profile on the retrievals.

481 Fig. 4a illustrates the distribution of the prior sensitivity analysis matrix (A_0) column vectors across the 12–40 km
482 altitude range, with each curve plotted at a vertical resolution of 2 km. A peak centered near the perturbation altitude
483 indicates that the retrieval at that altitude retains sensitivity to the prior value at the same level. The width of the peak
484 reflects the degree of vertical smoothing inherent in the retrieval. At the lower boundary (below 15 km), the response
485 amplitudes are weak, indicating that perturbations in the prior at these altitudes have limited influence on the retrieved
486 profile. This is consistent with the reduced information content of limb measurements in the upper troposphere and lower
487 stratosphere, where the retrieval is primarily constrained by the measurement geometry and cloud filtering rather than the
488 prior.

489 While Fig. 4a illustrates the pattern of prior influence, it does not quantify the actual retrieval error that would result
490 from an inaccurate prior. To assess this, the entire prior profile was uniformly scaled by +5% at all altitudes, and the
491 relative difference between the perturbed retrieval and the standard retrieval was computed. Fig. 4b shows the relative
492 error induced by a +5% perturbation of the prior profile. Below 20 km, the retrieval shows sensitivity to the a priori, with
493 relative errors -5% in tropical regions. This indicates that a small increase in the prior profile leads to a noticeable
494 underestimation of retrieved ozone concentrations in the tropical lower stratosphere, reflecting the high sensitivity of the
495 retrieval to prior information in this region where measurement information content is low. With increasing altitude, the
496 magnitude of the error progressively decreases. Above 25 km, the error approaches 0% across all latitudes. At high
497 latitudes, the error magnitude remains relatively small at all altitudes, indicating weaker prior dependence compared to
498 tropical and mid-latitude regions.

删除的内容: research

删除的内容: technology

删除的内容: DOAS and

删除的内容: .

删除的内容: T

删除的内容: are

删除的内容: Therefore

删除的内容:

删除的内容: the estimation of the total retrieval error of ozone profiles focuses on such factors as

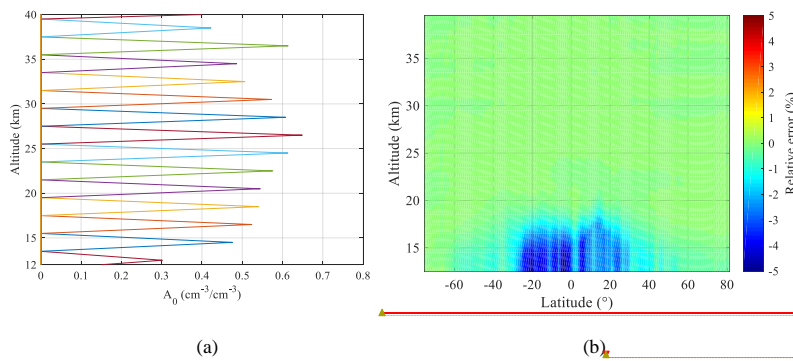
删除的内容: Understanding the impact of the initial ozone profile on retrieval results is crucial.

删除的内容: average kernel

删除的内容: 5a

删除的内容: average kernel

删除的内容: It indicates that at the lower boundary of retrieval, perturbations in the prior profile hardly induce significant responses in the retrieval results. Fig. 5b compares the relative retrieval errors under the conditions of prior profiles at low latitudes (5.5°S) and mid-latitudes (45°N), and it is found that the errors increase significantly at the lower boundary of retrieval, which is consistent with the analysis results of A_0 . The prior errors of retrieved ozone profiles above 20 km have weak correlation with latitude, and the errors remain at 1-2% in the altitude range of 20-40 km; while at lower altitudes, especially in tropical and mid-latitude regions, the relative errors can reach 10-25% due to the rapid decrease of ozone concentration and the reduction of retrieval accuracy.



带格式的: 字体: (默认) Times New Roman, 10 磅

538

539

540

541

542

543

544

545

546

547

548

549

550

551

552

553

554

555

556

557

558

559

560

561

562

563

564

565

566

567

Figure 4. Examples of A_0 (plotted every 2 km) and theoretical accuracy of prior profiles. (a) Distribution of A_0 for measurements at 2.2 \AA ; (b) Relative retrieval error resulting from a uniform +5% perturbation of the entire prior profile (orbit 51220 on September 15, 2021).

The uncertainty of stratospheric aerosol extinction coefficients must be considered in the error budget for ozone profile retrievals. Previous studies have shown that retrieved aerosol extinction profiles have an average upper error bound of approximately 30% in the lower stratosphere (Arosio et al., 2022). To assess the impact of this uncertainty on our ozone retrieval, we perturbed the climatological aerosol extinction profile by uniformly scaling it by +30% at all altitudes and repeated the retrieval. The relative difference between the perturbed retrieval and the standard retrieval was then computed. Fig. 5a depicts the resulting ozone retrieval errors as a function of latitude and altitude. It is evident that retrieval errors induced by variations in aerosol extinction coefficients are predominantly distributed within the 15-25 km altitude range, with a magnitude of approximately 5%, and errors in the southern high latitudes are more pronounced. Within the 25-30 km range, the error is around 2%, while above 30 km, it is less than 1%. Below 15 km, errors vary with latitude, mostly falling within the range of $\pm 2\%$.

The temperature dependence of ozone absorption cross-sections has the potential to introduce errors in the retrieved profiles. To assess this effect quantitatively, we followed the approach which applied a uniform +2% perturbations to the ozone absorption cross-sections at all temperatures used in the forward model. This perturbation magnitude represents a typical conservative estimate of cross-section uncertainty in the Chappuis band (Arosio et al., 2022). The retrieval was then repeated using the perturbed cross-sections, and the relative difference relative to the standard retrieval was computed.

As shown in Fig. 5b, the resulting retrieval error exhibits a distinct vertical and latitudinal structure. In the tropics, the largest negative deviations (-3% to -5%) appear below 20 km, indicating that retrievals in the tropical lower stratosphere are most sensitive to uncertainties in ozone absorption cross-sections. In the Southern Hemisphere (SH) mid-to-high latitudes, prominent negative deviations (-3% to -4%) are found below 26 km. In the Arctic region, the negative bias below 20 km is relatively smaller, at approximately -2%. Across all latitudinal bands, the error stabilizes near -2% above 25 km. These results confirm that uncertainties in ozone absorption cross-sections introduce systematic biases in lower stratospheric ozone retrievals, especially in the tropics and SH mid-to-high latitudes. Specifically, a positive perturbation in the cross-sections leads to an underestimation of ozone concentrations, as observed in the negative biases in Fig. 5b.

删除的内容:

带格式的: 字体: (默认) Times New Roman, 小五

带格式的: 字体: 加粗

带格式的: 缩进: 首行缩进: 0 字符

删除的内容: 5

删除的内容: Variation of retrieval errors of prior profiles in mid-latitudes and low latitudes with latitude

删除的内容: requires consideration

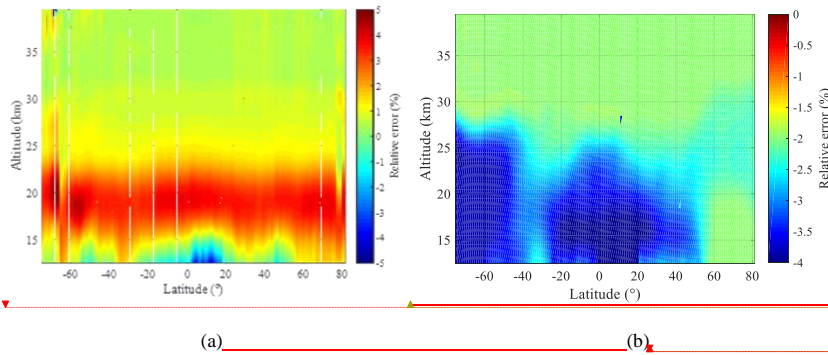
删除的内容: .

删除的内容: S

删除的内容: demonstrated

删除的内容: exhibit

删除的内容: Figure 6(a) illustrates the distribution characteristics of ozone retrieval errors with latitude and altitude under a 30% uncertainty in aerosol extinction coefficients.



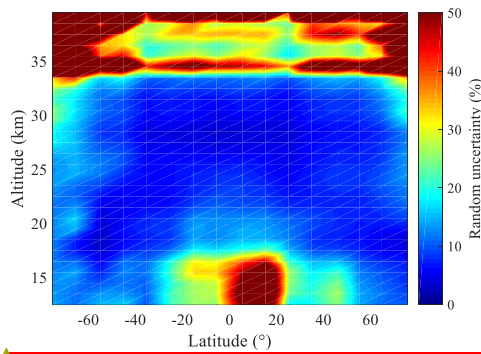
583

584

585 **Figure 5.** Distribution of relative errors in ozone retrieval with latitude and altitude, resulting from: (a) a +30% uniform perturbation of
 586 the aerosol extinction profile; (b) a +2% uniform perturbation of ozone absorption cross-sections at all temperatures.

587 To quantify the impact of random measurement noise on retrieval precision, a Monte Carlo simulation was
 588 performed using data from OMPS/LP orbit 51220. Sixteen representative latitudes spanning from 80°S to 80°N were
 589 selected. For each latitude, Gaussian random noise with a standard deviation of 1% was added independently at each
 590 tangent height to the retrieval vector y_j (Eq. 2). This process was repeated 100 times, generating 100 independent noisy
 591 realizations per latitude. A full MART retrieval was conducted for each realization, producing an ensemble of 100
 592 retrieved ozone profiles for each latitude. The random uncertainty due to measurement noise was quantified as the
 593 standard deviation of the 100 retrieved profiles at each altitude, expressed as a percentage of the average of the
 594 unperturbed profiles.

595 Fig. 6 shows the latitudinal and altitudinal distribution of the resulting random uncertainty. Uncertainty remains
 596 low (<10%) at most latitudes within the 20–33 km mid-stratosphere, reflecting robust and stable retrieval performance.
 597 Above 30 km, especially at high latitudes, uncertainty increases sharply to above 20%, which is mainly attributed to
 598 weaker signals in the visible spectral range. In the tropics below 20 km, a region of elevated uncertainty (>15%) is
 599 identified, likely associated with low ozone abundances, strong atmospheric variability, or reduced information content
 600 from the measurements.



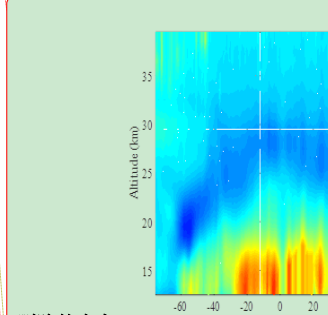
601

602 **Figure 6.** Random uncertainty in retrieved ozone profiles due to measurement noise, quantified as the standard deviation of 100 Monte
 603 Carlo realizations with 1% Gaussian noise added to the retrieval vector.

604

删除的内容: Since ozone absorption cross-sections depend solely on temperature rather than pressure, it is necessary to investigate the impact of the temperature sensitivity of absorption cross-sections on ozone profile retrieval. Figure 6(b) presents the relative errors in ozone retrieval caused by differences in ozone absorption cross-sections at 243K and 223K. Results show that when the temperature difference is 20K, the retrieval errors induced by ozone absorption cross-sections are less than 0.6% across all latitudes and altitudes, with the maximum error occurring below 18km in tropical regions. A 1% perturbation was added to the retrieval vector to simulate measurement noise, and the resulting relative errors in ozone retrieval were calculated. As shown in Figure 6(c), retrieval errors...

带格式的: 字体: (默认) Times New Roman, 10 磅



删除的内容: ...

带格式的: 字体: (默认) Times New Roman, 小四

带格式的: 字体: 小五

删除的内容: (a)
(b) (c)

删除的内容: 6

删除的内容: . (a) Aerosol extinction coefficients; (b) Ozone absorption cross-sections; (c) Measurement noise.

带格式的: 字体: (默认) Times New Roman, 小五, 字体颜色: 蓝色

665 **4.2 Comparison with NASA OMPS-LP ozone product**

666 The OMPS/LP v2.6 ozone profile retrieval algorithm developed by the NASA team is built on wavelength pairing
 667 and an optimal estimation with prior constraints (Kramarova and Deland, 2023). This algorithm operates on combined
 668 UV-Vis measurement data from 12.5 km (or cloud top) to 57.5 km, producing a single ozone profile from each retrieval.
 669 The measurement vectors are obtained via doublet and triplet methods, with specific parameters detailed in Table 1.
 670 During algorithm implementation, the retrieved surface albedo, cloud top height, and corrected TH are integrated. In the
 671 forward model, aerosol extinction coefficients retrieved from OMPS/LP measured data are used.

672 **Table 1.** Parameters used in the OMPS/LP v2.6 ozone algorithm, according to Kramarova and Deland, (2023).

Parameters	Values
Wavelength used in UV (nm)	295, 302, 306, 312, 317, 322, 353
Wavelength used in Vis (nm)	510, 606, 675
Normalization Altitude in UV (km)	60.5 km
Normalization Altitude in Vis (km)	40.5 km

673 Fig. 7 shows a comparison between the retrievals of this study and those of OMPS/LP v2.6, involving
 674 approximately 770,000 profiles. Among them, Fig. 7a presents an example of number density for the annual average
 675 profile, and Fig. 7b shows the relative differences of the annual data. In this study, the relative difference is calculated as
 676 follows:

677
$$E_{\text{dif}} = \frac{2 \cdot ([O_3]_{\text{Ret}} - [O_3]_{\text{Ref}})}{([O_3]_{\text{Ret}} + [O_3]_{\text{Ref}})} \times 100\% \quad (7)$$

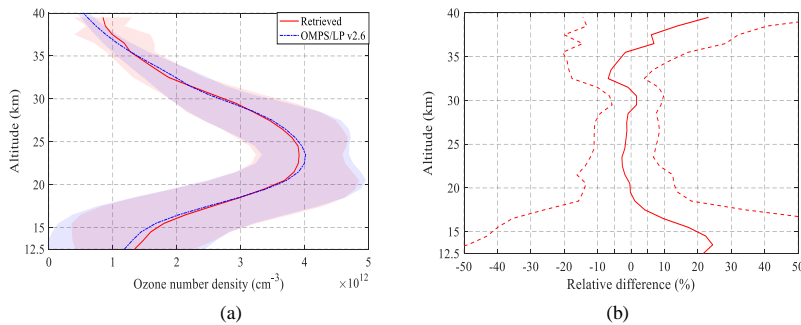
678 where $[O_3]_{\text{Ret}}$ denotes the ozone profile retrieved in this study, and $[O_3]_{\text{Ref}}$ represents the reference ozone profile
 679 product.

680 As presented in Fig. 7b, the ozone concentrations from our retrieval systematically exceed those of the OMPS/LP
 681 v2.6 product at altitudes below 19 km and above 35 km. The positive deviation increases with decreasing altitude,
 682 reaching a maximum of approximately 10–24% at the upper and lower boundaries of retrieval. The ozone concentration
 683 is slightly lower between 20 and 28 km, with a deviation within 3%. There is an inherent negative deviation of about -6%
 684 around ~33 km. Overall, the deviation between 17 and 36 km is confined within 5%.

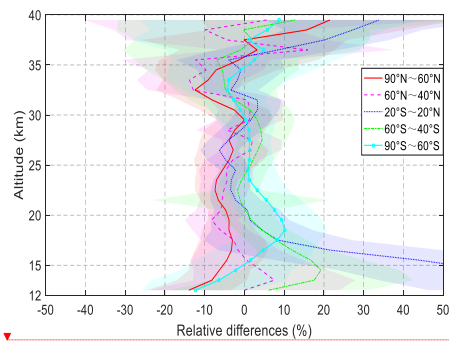
685 Fig. 8 shows the mean relative differences, between the retrievals of this study and OMPS/LP v2.6 in tropical
 686 regions and southern, northern mid-high latitudes. In the tropical regions within the 18-36 km altitude range, the
 687 deviation is within 5%, showing good consistency. At northern mid-high latitudes, the difference between 12 and 32 km
 688 reaches 8%, and the difference above 32 km is as high as 8–13%, with similar deviations in the Arctic region. In the
 689 southern mid-high latitudes, most of the deviations above 18 km are less than 3%, but there is a positive deviation of up
 690 to 19% near 15 km. In the Antarctic region, this positive deviation reaches approximately 10% around 18 km.

691 The two datasets differ significantly in the upper troposphere and lower stratosphere (UTLS) region, especially in
 692 the tropical region, mainly due to the extremely low ozone concentration at this altitude. The large positive deviation at
 693 the upper boundary of retrieval may be caused by the decreased ability of the visible spectrum to retrieve ozone at high
 694 altitudes, while the NASA product uses combined ultraviolet and visible spectrum information for retrieval at this
 695 altitude. Although there are differences between the retrievals of this study and the OMPS/LP v2.6 product in terms of
 696 ozone absorption cross-sections, prior profiles, aerosol settings, retrieval algorithms, and spectra, the overall consistency
 697 is high.

- 删除的内容: controlled
- 删除的内容: comparison
- 删除的内容: region
- 删除的内容: In the northern mid-latitude region
- 删除的内容: extends to around 18 km,
- 删除的内容: profiles
- 删除的内容: in low latitudes



706
707
708 **Figure 7.** (a) Annual mean ozone number density profiles from this study and OMPS/LP v2.6, with shaded areas indicating the
709 standard deviation. (b) The corresponding annual mean relative differences calculated pairwise for each collocated measurement using
710 Eq. (7), with the standard deviation shown as a dashed line.



711
712 **Figure 8.** Zonal mean relative differences (this study vs. OMPS/LP v2.6) across five latitudinal bands (60°-90°N, 40°-60°N, 20°S-
713 20°N, 60°S-40°S and 90°S-60°S), with corresponding standard deviations as shaded areas.

714 4.3 Comparison with MLS

715 The Earth Observing System-Microwave Limb Sounder (EOS-MLS) aboard the Aura satellite was successfully
716 launched on July 15, 2004 (Waters et al., 2006). The satellite completes about 14 orbits daily, achieving global coverage
717 between 82°S and 82°N. The MLS obtained vertical ozone profiles from the upper troposphere to the middle atmosphere
718 using the 240 GHz frequency band by detecting naturally emitted microwave thermal radiation from the Earth's
719 atmospheric limb measurements. Detailed descriptions can be found by Waters et al. (2006).

720 For validation purposes, this study employs the latest MLS L2 version 5.0 data product (Schwartz et al., 2020), with
721 data filtering applied in accordance with the protocols recommended by Livesey et al. (2022). To ensure collocation
722 quality from the dataset, stringent criteria were enforced: we retained only those data pairs where the geographical
723 separation between the OMPS/LP and MLS footprints was within 1° in both latitude and longitude, and the observation
724 time difference was less than 6 hours. In cases where multiple MLS profiles corresponded to a single OMPS/LP
725 measurement, their average was computed and used. For consistent comparison with NASA products and ozonesonde
726 data, the MLS volume mixing ratio (VMR) and pressure were first transformed to number density and altitude, utilizing
727 the MLS geopotential height and temperature. These converted profiles were subsequently interpolated onto the regular
728 altitude grid of the OMPS retrievals using a spline method.

729 Fig. 9 presents the average profiles and relative differences between the retrieval results of this study and MLS v5.0,
730 involving approximately 93,000 profiles. The results show that compared with MLS v5.0, the ozone concentration

带格式的: 字体: 小五

带格式的: 字体: (默认) Times New Roman, 小五

删除的内容: The corresponding annual mean relative differences

删除的内容:

带格式的: 居中

删除的内容: (a, b) Retrieved and OMPS/LP v2.6 ozone number density profiles averaged in the tropical region and Antarctic. (c) The

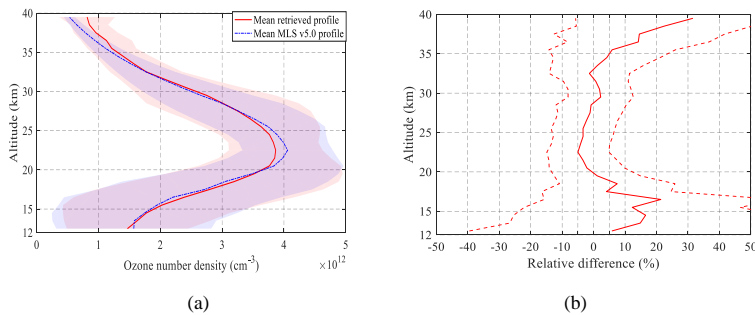
删除的内容: are shown in

删除的内容: operates along

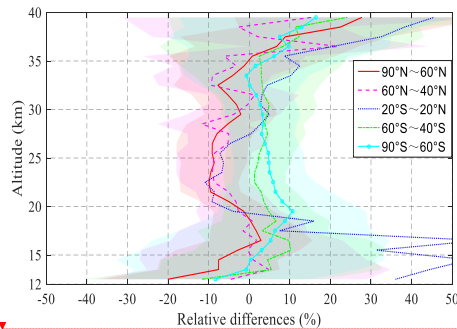
删除的内容: substantial

742 retrieved in this study has a relatively large positive deviation of 5–20% below 18 km; the positive deviation above 32
 743 km increases with altitude; within the 18–35 km height range, the deviation between the two is confined within 5%.

744 Fig. 10 shows the mean relative differences in five latitude zones, with shaded areas indicating the standard
 745 deviations. In terms of data sample size, there are approximately 18,000 profiles in the tropical region, about 20,000 in
 746 the northern high latitudes, and around 15,000 in the southern high latitudes. The analysis results reveal that within the
 747 12–35 km height range, the zonal average relative differences in each latitude zone are basically confined within 10%.
 748 Among them, the northern mid-high latitudes exhibit a stable negative deviation of 5–10% at 20–35 km; the southern
 749 mid-latitudes have a constant positive deviation of 1–5% at 18–36 km, which increases to 3–10% in the polar regions. the
 750 tropical regions the differences change sign with altitude; the retrieved ozone number density at 19–27 km is 5–10%
 751 lower than that of MLS, while it is 3–10% higher in the 28–36 km range. It is worth noting that below 19 km, the
 752 consistency between the retrieval results of this study and MLS data decreases significantly, with the relative difference
 753 in the tropical region even exceeding 30%, although the absolute difference is relatively small (see Fig. 10a).



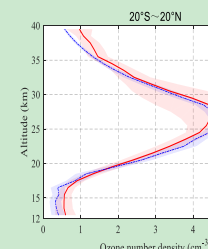
754
 755
 756 **Figure 9.** (a) Annual mean ozone number density profiles from this study and MLS v5.0, accompanied by standard deviations (shaded
 757 areas). (b) The corresponding annual mean relative differences calculated pairwise for each collocated measurement using Eq. (7),
 758 with the standard deviation shown as a dashed line.



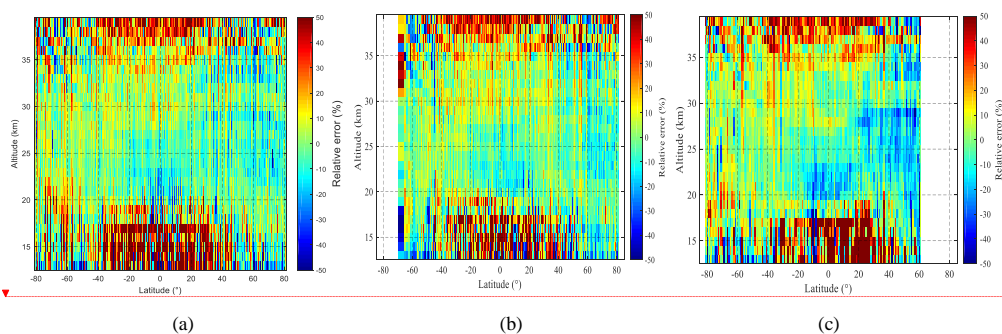
759
 760 **Figure 10.** Zonal mean relative differences (this study vs. MLS v5.0) across five latitudinal bands (60°–90° N, 40°–60° N, 20°S–20° N,
 761 60°–40° S and 90°–60° S), with corresponding standard deviations as shaded areas.

762 Fig. 11 presents the variation of relative differences between retrieval profiles within 1° latitude bins and MLS zonal
 763 averages with altitude, covering three time periods. The full-year 2021 data shown in Fig. 11a indicate that within the
 764 20–35 km altitude range, differences across all latitudes are basically confined within ±10%. The altitude-dependent
 765 behavior of the retrieval biases can be summarized as follows. In the tropical UTLS region, oscillating differences
 766 exceeding 30% are observed, which may be attributed to several factors: the highly dynamic variability of ozone
 767 concentration, the limited detection sensitivity at the lowest retrieval altitude, the influence of cloud filtering.
 768 Furthermore, the inherently low ozone abundance, in this region exacerbates retrieval uncertainties. A distinct negative

768 Furthermore, the inherently low ozone abundance, in this region exacerbates retrieval uncertainties. A distinct negative

- 删除的内容: the increase
- 删除的内容: controlled
- 删除的内容: the average profiles in the tropics and southern high latitudes, as well as
- 删除的内容: controlled
- 删除的内容: further expand
- 删除的内容: The tropical region shows obvious stratification characteristics
- 删除的内容: The corresponding annual mean relative differences, accompanied by standard deviations (dashed lines).
- 删除的内容: 
- 删除的内容: (a) Retrieved and MLS v5.0 ozone number density profiles
- 删除的内容: are shown in
- 删除的内容: controlled
- 删除的内容: Analyzing the difference characteristics from low to high
- 删除的内容: the tropical UTLS region, which may be caused by factors such
- 删除的内容: changes in
- 删除的内容: insufficient
- 删除的内容: in
- 删除的内容: segment, and cloud filtering effects; in addition
- 删除的内容: concentration
- 删除的内容: also affects the accuracy of retrieval profiles

813 bias in retrieved ozone values is evident at 20–23 km in the tropics, particularly pronounced during winter (Fig. 11c).
 814 Conversely, a positive bias is observed over Antarctica, possibly linked to biases in surface albedo retrieval at high
 815 southern latitudes during polar winter. Above 35 km, the retrievals exhibit a positive bias in the tropics. This altitude
 816 range coincides with the transition zone between ultraviolet and visible spectral windows, where inconsistencies in the
 817 merging of data from these two spectral regions may contribute to the observed discrepancies.



818
 819
 820 **Figure 11.** Relative differences in ozone number density, averaged over 1° latitude bins and plotted as a function of altitude, for (a) the
 821 entire year of 2021, (b) the boreal summer months (June-August), and (c) December.

822 In summary, the comparative analysis of this study shows that the effectiveness of OMPS retrieval varies across
 823 different regions and altitudes: the accuracy in tropical regions is concentrated in the 20-35 km altitude range; in
 824 mid-latitude regions, good consistency is also observed below 15 km. Nevertheless, in some atmospheric regions and
 825 under different seasonal conditions, the relative deviation may still exceed 10% compared with MLS data.

删除的内容: In the tropical region, there is a decreasing trend in retrieved ozone values at 20-23 km altitude, which is particularly significant in winter (see Fig. 11c); while higher values are observed in the Antarctic region, which may be related to albedo retrieval deviations at polar latitudes in winter. Above 35 km, retrievals in the tropical region are larger, and this interval corresponds to the overlapping area of ultraviolet and visible spectral

删除的内容: windows, where the merging of data from the two may cause inconsistent results.

删除的内容: effectiveness

826 **4.4 Comparison with OSIRIS**

827 In February 2001, the OSIRIS instrument was launched aboard the Odin satellite into a nearly circular
 828 sun-synchronous orbit (Llewellyn et al., 2004). The orbit has an altitude of approximately 600 km, an orbital period of 96
 829 minutes, an inclination of 97.8°, and covers an observational latitude range from 82°S to 82°N. The satellite's ascending
 830 node crosses the equator at approximately 18:00 local time. Detailed descriptions of the instrument can be found by
 831 Llewellyn et al., (2004). Degenstein et al. (2009) used the MART to retrieve ozone profiles in the altitude range from 10
 832 km or cloud top to 60 km, with the retrieval algorithm integrating radiation information from the UV and VIS bands. In
 833 this study, the version of OSIRIS L2 v7.3 data (University of Saskatchewan, 2025) is used for verification.

834 Owing to the sparsity of coincident OSIRIS measurements, a relaxed collocation criterion was adopted. Data pairs
 835 were considered matched if the geographical distance between the instrument footprints was within 2° in latitude and 5°
 836 in longitude, and the time difference was within 24 hours. When multiple OMPS/LP profiles corresponded to a single
 837 OSIRIS observation, their average was used. To unify the data format, the ozone concentration unit (mol/m³) of OSIRIS
 838 profiles is converted to number density (/cm³).

839 Fig. 12 shows the average profiles and relative differences between the retrieval results of this study and OSIRIS
 840 v7.3, involving approximately 44,000 profiles. The results indicate that compared with OSIRIS v7.3, the ozone
 841 concentration retrieved in this study has a relatively large positive deviation of 28-34% below 18 km; above 35 km, the
 842 positive deviation increases with increasing altitude; in the 20-35 km altitude range, except near 23 km, most of the
 843 deviations between the two are confined within 5%.

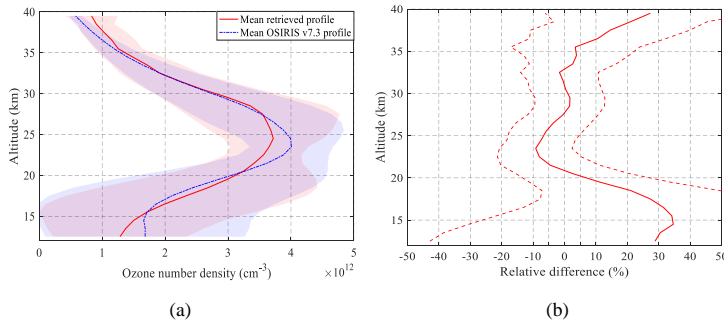
844 Fig. 13 further compares the mean relative differences of the five latitude zones, with shaded areas indicating the
 845 standard deviations. In terms of data sample size, there are approximately 17,000 profiles in the tropical region, about
 846 10,000 in the northern high latitudes, and around 7,000 in the southern high latitudes. The analysis shows that the

删除的内容: controlled

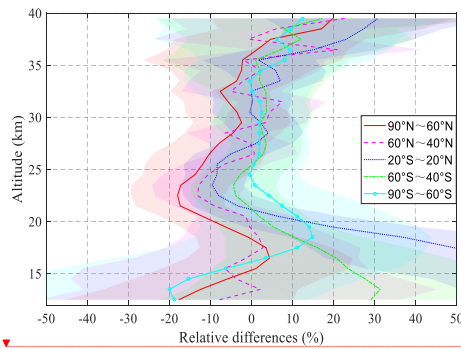
删除的内容: average profiles in the tropics and southern high latitudes, as well as

删除的内容: the

868 northern mid-high latitudes have a significant negative deviation of 5-13% at 21-25 km altitude, which is more prominent
 869 in polar regions; the difference in the southern mid-latitudes at 20-36 km altitude is less than 4%, and the consistency in
 870 the Antarctic region at 23-35 km altitude is better than 2.5%; most of the deviations in the tropical region at 26-36 km
 871 altitude are within 2%. In addition, the differences in the region below 20 km are significant, with the relative difference
 872 in the tropical region exceeding 50% and reaching 30% at 13 km in the southern mid-latitude zone.



873
 874 **Figure 12.** (a) Annual mean ozone number density profiles from this study and OSIRIS v7.3, accompanied by standard deviations
 875 (shaded areas); (b) **The corresponding annual mean relative differences calculated pairwise for each collocated measurement using Eq.**
 876 **(7), with the standard deviation shown as a dashed line.**
 877



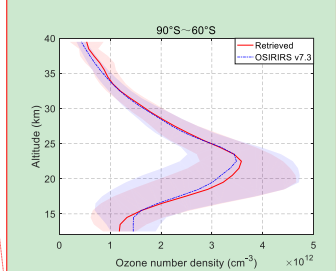
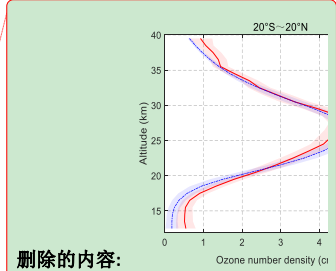
878
 879 **Figure 13.** Zonal mean relative differences (**this study vs. OSIRIS v7.3**) for five latitudinal bands (60°-90°N, 40°-60°N, 20°S-20°N,
 880 60°-40°S and 90°-60°S); standard deviations as shaded areas.

881 4.5 Comparison with ozonesondes

882 To robustly validate the retrieved ozone concentrations at altitudes below 30 km, this study employs a comparative
 883 analysis with ozonesonde measurements. The sonde data were obtained from the World Ozone and Ultraviolet Radiation
 884 Data Centre (WOUDC) and the Southern Hemisphere Additional Ozonesondes (SHADOZ) network (Thompson et al.,
 885 2007). Accounting for the sparse spatial distribution of ozonesonde stations, a relaxed collocation criterion was
 886 implemented: an OMPS/LP measurement was considered a match if it fell within ±5° latitude and ±10° longitude of a
 887 sonde station and occurred within ±12 hours of its launch. For each ozonesonde profile, all collocated OMPS/LP
 888 retrievals were averaged to form a single comparative data point.

889 In quantitative comparisons, to align the vertical resolution of ozonesonde data with that of OMPS data, a moving
 890 average filtering method is used for dimensionality reduction of ozonesonde data. The specific procedure begins with
 891 defining the window size of the moving average filter:

删除的内容: The corresponding annual mean relative differences, accompanied by standard deviations (dashed lines).



带格式的: 居中

删除的内容: (a, b) Annual mean ozone number density profiles (this study vs. MLS v5.0) for the tropics and Antarctic, respectively. (c)

902
$$N = \frac{\Delta z_{\text{low}}}{\Delta z_{\text{high}}} \quad (8)$$

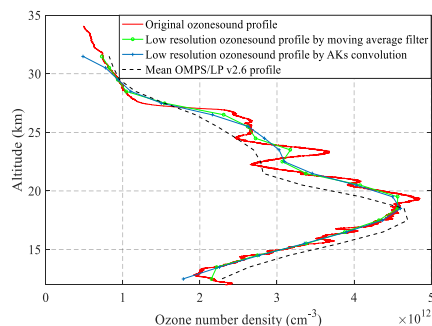
903 where, Δz_{low} and Δz_{high} represent the low vertical resolution of OMPS data and the high vertical resolution of
 904 ozonesonde data, respectively.

905 Filtering is applied to the original ozonesonde data x_{fine} to obtain the dimensionality-reduced data x_{coarse} , which
 906 is expressed as:

907
$$x_{\text{coarse}}(z_k) = \frac{1}{2N+1} \sum_{j=-N}^N x_{\text{fine}}(z_{k+j}) \quad (9)$$

908 where z_k denotes the altitude, and k represents the layer index.

909 In addition, another processing approach involves convolving ozonesonde measurements with the averaging kernels
 910 (AKs) retrieved from OMPS/LP v2.6 (see Arosio et al., (2018) for details). Taking the Alert station (82.5 °N, 62.4 °W) as
 911 an example, Fig. 14 presents the comparison results between the ozonesonde data and the collocated OMPS average
 912 profile on September 15, 2021. It is found that there are differences in the dimensionality-reduced ozonesonde data
 913 obtained by the two methods. The data curve processed by convolution with averaging kernels is smoother and its shape
 914 is closer to the OMPS product; while the data processed by moving average filter retains more original features with a
 915 sharper curve. After comprehensive consideration, the moving average filter is finally adopted for data processing in this
 916 study.



917 **Figure 14.** Ozonesonde data and OMPS collocated average profile at Alert station on September 15, 2021.

918 Fig. 15 presents the annual average collocated profiles and their relative differences. The left side of the figure
 919 indicates the number of valid collocations at each altitude, with the total sample size amounting to approximately 1460.
 920 This study included data from 41 ozonesonde stations, involving over 1700 individual profiles. A significant positive bias
 921 of 10–15% is observed in the retrievals compared to ozonesonde data below 18 km, while the deviation generally stays
 922 within 10% across the 15–30 km altitude range.

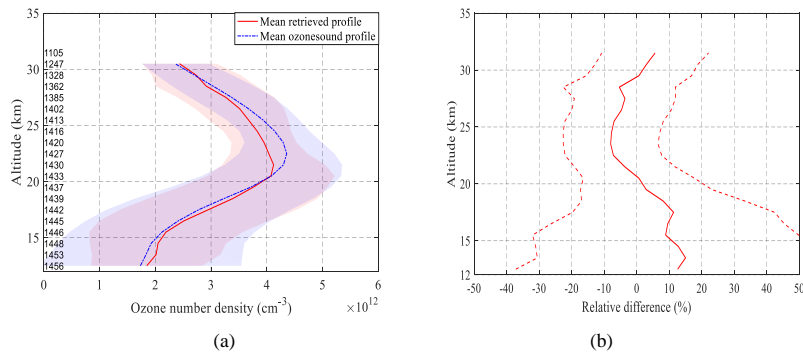
923 Fig. 16 presents the mean relative differences across five latitude zones. The number of available collocations in the
 924 tropical and Antarctic regions is approximately 200 and 75, respectively. Specifically, the tropical region shows good
 925 consistency above 20 km, with most relative differences within $\pm 4\%$ between 20 and 30 km. The southern mid-latitude
 926 region also exhibits high consistency, with positive biases generally less than 5% above 20 km, but a relatively large
 927 positive bias of about 19% near 15 km. In the Antarctic region, the bias is less than 2% above 25 km, while significant
 928 differences occur below 25 km, with a positive bias as high as 21% at 19 km. The northern mid-latitude zone has a bias
 929 of less than 5% below 21 km, but a constant negative bias of 5–11% between 21–28 km, and this negative bias are more
 930 pronounced in the Arctic region.

删除的内容: Figure

删除的内容: denotes

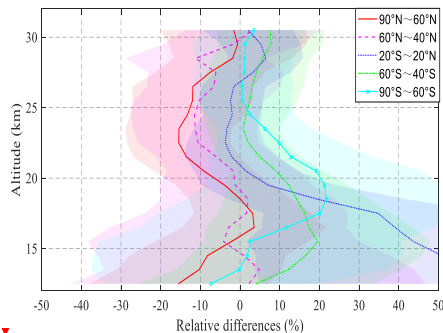
删除的内容: average collocated profiles in the tropical and Antarctic regions, as well as the relative differences across five latitude zones

删除的内容: The left side of the figure indicates that the number of available collocations in the tropical and Antarctic regions is approximately 200 and 75, respectively



943
944
945
946
947

Figure 15. (a) Annual mean collocated ozone number density profiles from this study and ozonesonde measurements, accompanied by standard deviations (shaded areas). (b) Mean relative differences calculated pairwise for each collocated measurement using Eq. (7), with the standard deviation shown as a dashed line.



948
949
950

Figure 16. Zonal mean relative differences (this study vs. ozonesondes) for five latitudinal bands (60°-90°N, 40°-60°N, 20°S-20°N, 60°-40°S and 90°-60°S); standard deviations as shaded areas.

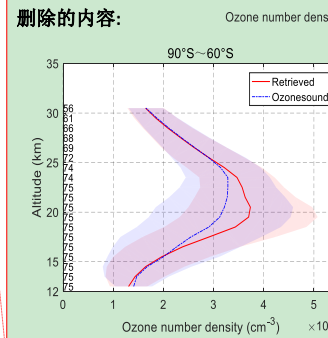
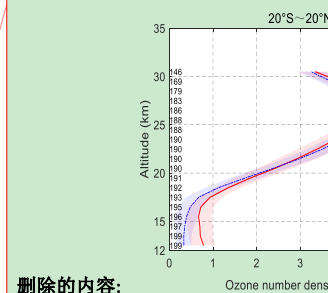
951 5. Conclusions

952 This study innovatively applies the ozone profile retrieval method—originally developed at the University of
953 Saskatchewan for OSIRIS measurements and based on wavelength pairing and the MART—to OMPS/LP observations.
954 After processing and analyzing the 2021 annual OMPS/LP v2.6 L1G data, observations with the instrument's central slit
955 and solar zenith angle less than 85° were selected, and ozone profiles between 12.5 and 39.5 km were retrieved. A
956 comprehensive multi-dimensional validation was conducted.

957 Comparison with the NASA L2 v2.6 official product shows that the overall consistency is good across latitude zones
958 at 20-36 km, with most differences within $\pm 5\%$. However, differences near 33 km in the northern mid-latitudes and polar
959 regions reach up to 10%. Below 20 km, ozone concentrations are relatively high in the Antarctic ozone peak region, with
960 a pronounced positive bias around 15 km in tropical and southern mid-latitude zones.

961 Validation against MLS v5.0 and OSIRIS v7.3 ozone profiles, as well as ozonesonde data from SHADOZ and
962 WOUDC, indicates that relative differences with MLS are mostly within $\pm 10\%$ between 13-35 km, except for significant
963 discrepancies in the tropical UTLS region. Compared to OSIRIS v7.3, a negative bias of 13-18% occurs at 20-25 km in
964 northern mid-high latitudes, while positive biases reach 18% at 18 km over Antarctic and exceed 20% at 15 km in
965 southern mid-latitudes, with more pronounced deviations in the tropics. Relative to ozonesonde data, differences in

删除的内容: The corresponding annual mean relative differences, accompanied by standard deviations (dashed lines).



带格式的: 居中

删除的内容: (a, b) Annual mean collocated ozone number density profiles (retrieval vs. ozonesondes) for the tropics and Antarctic,

删除的内容: respectively. (c)

977 tropical and southern mid-latitude regions at 20-30 km remain within $\pm 4\%$, whereas differences of 11-15% are observed
978 at 20-25 km in northern mid-high latitudes. Consistency is good below 20 km in northern mid-latitudes, but positive
979 biases reach 21% at 18 km over Antarctica and 19% at 15 km in southern mid-latitudes.

980 Overall, compared with the reference products, the retrieved ozone concentrations in this study exhibit biases mostly
981 within 5% between 25 and 35 km. A negative bias of 5-10% is observed at 20-25 km in northern mid-high latitudes,
982 particularly in the Arctic. Retrieved values are about 10% higher at the altitude of the Antarctic ozone concentration peak,
983 10–15% higher at 15 km in southern mid-latitudes, and over 30% higher below 20 km in the tropics.

984 The identified biases mainly originate from three factors. Below 20 km, cloud effects remain non-negligible. Even
985 after excluding cloud-affected radiances, retrievals of lower-altitude ozone profiles are still constrained by the initial
986 profile, as no iterative update is applied below the detected cloud top height. Consequently, ozone abundances above
987 cloud tops are overestimated by more than 25%. These discrepancies are further exacerbated by low ozone abundance,
988 strong dynamical variability in the tropics, and the reduced sensitivity of limb retrievals at lower altitudes, while
989 inconsistencies between the background aerosols used in retrievals and real atmospheric conditions also contribute. The
990 overestimation of ozone abundances above 35 km across all latitudes results from the limited sensitivity of the visible
991 spectrum for high-altitude ozone retrievals, in contrast to the operational product that employs combined ultraviolet and
992 visible spectral information.

993 Based on these findings, several priorities for follow-up research are identified. First, integrating operational aerosol
994 extinction products from NASA will be essential to replace the current climatological approach and reduce systematic
995 biases in the UTLS region. Second, including ultraviolet channels will improve retrieval accuracy above 35 km, where
996 visible-only measurements have low sensitivity. Third, refining cloud filtering will better constrain lower altitude
997 retrievals. Finally, the consistent retrieval core shared with OSIRIS lays a solid technical foundation for constructing
998 long-term, coherent stratospheric ozone records, thereby minimizing discrepancies in multi-satellite data merging and
999 supporting climate studies that require stable, multi-decadal observational records.

删除的内容: -

删除的内容: and the adjustment factor above clouds, leading to ozone concentrations more than 25% higher above cloud tops. Inaccurate prior profiles in the mid- to low latitude regions introduce retrieval biases exceeding 20%, while low ozone abundance, strong dynamical variability in the tropics, and reduced sensitivity of limb retrievals further exacerbate discrepancies. Additionally, differences between the background aerosols used in retrievals and real atmospheric conditions also contribute. The elevated concentrations above 35 km across latitude zones result from the limited capability of visible spectra for high-altitude ozone, retrieval, unlike the official product, which uses combined ultraviolet and visible spectra.

删除的内容: Based on error analysis, follow-up research will focus on optimizing the retrieval algorithm, adopting more realistic prior profiles, and constraining the retrieval altitude to cloud-top height. Efforts will also be directed toward deriving aerosol profiles from limb radiance measurements to improve the forward model. This study successfully demonstrates the feasibility of applying the wavelength pairing and MART technique to OMPS/LP ozone profile retrieval, laying a solid technical foundation for broader application of this approach. It also underscores the importance of consistent retrieval settings for constructing long-term, coherent stratospheric ozone datasets and minimizing discrepancies in multi-satellite data merging. .

1000 **Data availability**

1001 Ancillary information and v2.6 L1G OMPS/LP data were downloaded from <https://disc.gsfc.nasa.gov/datasets>
1002 (NASA, 2025a), where L2 data are also available. For the validation sections, MLS L2 data were also taken from <https://disc.gsfc.nasa.gov/datasets> (Schwartz, et al., 2020). OSIRIS v7.3 data were taken from <https://research-groups.usask.ca/osiris/data-products.php> (University of Saskatchewan, 2025). WOUDC data were
1003 downloaded on 10 April 2025 from <https://woudc.org/data/explore.php>. A list of all contributors is available on the
1004 following website: <https://woudc.org/contributors/>. SHADOZ data were downloaded on 21 April 2025 from
1005 <https://tropo.gsfc.nasa.gov/shadoz/Archive>. Html (NASA, 2025b).

1008 **Author contributions**

1009 FZ designed the retrieval algorithm to OMPS/LP observations, processed the data set, performed the validation of
1010 the results and wrote the manuscript. FZ and SWL proposed the research and lead the project, analyzed the results and
1011 contributed to the writing of the manuscript and the scientific outcomes. XPL contributed the algorithm for cloud filtering,
1012 and reviewed the paper. FQS supervised and guided the retrieval process and reviewed the paper.

1057 **Competing interests**

1058 The authors declare that they have no conflict of interest.

1059 **Acknowledgements**

1060 This work was supported by the National Science Foundations of China (Grant No. 41875040), and partially funded
1061 by the Excellent Research and Innovation Team of Anhui Provincial Department of Education (2023AH010043)

1062 We would like to express our sincere gratitude to the NASA OMPS SIPS team for providing data support. We are
1063 also [thankful](#) to the SCIATRAN radiative transfer model development team.

删除的内容: thanks

1064 **References**

- 1065 Arosio, C., Rozanov, A., Malinina, E., Eichmann, K., von Clarmann, T., and Burrows, J. P.: Retrieval of ozone profiles
1066 from OMPS limb scattering observations, *Atmos. Meas. Tech.*, 11, 2135–2149,
1067 <https://doi.org/10.5194/amt-11-2135-2018>, 2018.
- 1068 Arosio, C., Rozanov, A., Gorshchev, V., Laeng, A., and Burrows, J. P.: Assessment of the error budget for stratospheric
1069 ozone profiles retrieved from OMPS limb scatter measurements, *Atmos. Meas. Tech.*, 15, 5949–5967,
1070 <https://doi.org/10.5194/amt-15-5949-2022>, 2022.
- 1071 Bernath, P. F., McElroy, C. T., Abrams, M. C., Boone, C. D., Butler, M., Camy-Peyret, C., Carleer, M., Clerbaux, C.,
1072 Coheur, P. F., Colin, R., DeCola, P., De Mazière, M., Drummond, J. R., Dufour, D., Evans, W. F. J., Fast, H., Fussen,
1073 D., Gilbert, K., Jennings, D. E., Llewellyn, E. J., Lowe, R. P., Mahieu, E., McConnell, J. C., McHugh, M., McLeod, S.
1074 D., Michaud, R., Midwinter, C., Nassar, R., Nichitiu, F., Nowlan, C., Rinsland, C. P., Rochon, Y. J., Rowlands, N.,
1075 Semeniuk, K., Simon, P., Skelton, R., Sloan, J. J., Soucy, M.-A., Strong, K., Tremblay, P., Turnbull, D., Walker, K. A.,
1076 Walkty, I., Wardle, D. A., Wehrle, V., Zander, R., and Zou, J.: Atmospheric Chemistry Experiment (ACE): Mission
1077 overview. *Geophysical research letters*, 32, L15S01, <https://doi.org/10.1029/2005GL022386>, 2005.
- 1078 Bertaux, J. L., Kyrola, E., Fussen, D., Hauchecorne, A., Dalaudier, F., Sofieva, V., Tamminen, J., Vanhellemont, F.,
1079 Fanton d'Andon, O., Barrot, G., Mangin, A., Blanot, L., Lebrun, J. C., Perot, K., Fehr, T., Saavedra, L., Leppelmeier,
1080 G. W., and Fraisse, R.: Global ozone monitoring by occultation of stars: an overview of GOMOS measurements on
1081 ENVISAT, *Atmos. Chem. Phys.*, 10, 12091–12148, <http://doi.org/10.5194/acp-10-12091-2010>, 2010.
- 1082 Bogumil, K., Orphal, J., and Burrows, J. P.: Temperature dependent absorption cross sections of O₃, NO₂, and other
1083 atmospheric trace gases measured with the SCIAMACHY spectrometer, in: *Proceedings of the*
1084 *ERS-Envisat-Symposium*, Goteborg, Sweden, 2000.
- 1085 Burrows, J., Häßle, E., Goede, A., Visser, H., and Fricke, W.: SCIAMACHY–Scanning imaging absorption spectrometer
1086 for atmospheric chartography, *Acta Astronautica*, 35, 445–451, [https://doi.org/10.1016/0094-5765\(94\)00278-T](https://doi.org/10.1016/0094-5765(94)00278-T), 1995.
- 1087 Cisewski, M., Zawodny, J., Gasbarre, J., Eckman, R., Topiwala, N., Rodriguez-Alvarez, O., Cheek, D., Hall S.: The
1088 Stratospheric Aerosol and Gas Experiment (SAGE III) on the International Space Station (ISS) Mission, in:
1089 *Proceedings 9241, Sensors, Systems, and Next-Generation Satellites XVIII, SPIE Remote Sensing*, Amsterdam,
1090 Netherlands, <https://doi.org/10.1117/12.2073131>, 2014.
- 1091 Chen, Z., DeLand, M., and Bhartia, P. K.: A new algorithm for detecting cloud height using OMPS/LP measurements,

1093 Atmos. Meas. Tech., 9, 1239–1246, <https://doi.org/10.5194/amt-9-1239-2016>, 2016.

1094 Chipperfield, M. P. and Bekki, S.: Opinion: Stratospheric ozone–depletion, recovery and new challenges, Atmos. Chem.

1095 Phys., 24, 2783–2802, <https://doi.org/10.5194/acp-24-2783-2024>, 2024.

1096 Degenstein, D. A., Bourassa, A. E., Roth, C. Z., and Llewellyn, E. J.: Limb scatter ozone retrieval from 10 to 60 km

1097 using a multiplicative algebraic reconstruction technique, Atmos. Chem. Phys., 9, 6521–6529,

1098 <https://doi.org/10.5194/acp-9-6521-2009>, 2009.

1099 DeLand, M., Bhartia, P., Xu, P., Kramarova, N., and Zhu, T.: OMPS Limb Profiler Ozone Product O₃: Version 2.5 Data

1100 Release Notes, 2017.

1101 Flittner, D. E., Bhartia, P. K., and Herman, B. M.: O₃ Profiles Retrieved from Limb Scatter Measurements: Theory,

1102 Geophysical research letters, 27(17), 2601–2604, <https://doi.org/10.1029/1999GL011343>, 2000.

1103 Flynn, L., Long, C., Wu, X., Evans, R., Beck, C., Petropavlovskikh, I., McConville, G., Yu, W., Zhang, Z., Niu, J., Beach,

1104 E., Hao, Y., Pan, C., Sen, B., Novicki, M., Zhou, S., and Sefstor, C.: Performance of the ozone mapping and profiler

1105 suite (OMPS) products, J. Geophys. Res.-Atmos., 119, 6181–6195, <https://doi.org/10.1002/2013JD020467>, 2014.

1106 Jia, J., Rozanov, A., Ladstätter-Weissenmayer, A., and Burrows, J. P.: Global validation of SCIAMACHY limb ozone data

1107 (versions 2.9 and 3.0, IUP Bremen) using ozonesonde measurements, Atmos. Meas. Tech., 8, 3369–3383,

1108 <https://doi.org/10.5194/amt-8-3369-2015>, 2015.

1109 Jaross, G., Bhartia, P. K., Chen, G., Kowitz, M., Haken, M., Chen, Z., Xu, P., Warner, J., Kelly, T.: OMPS Limb Profiler

1110 instrument performance assessment, J. Geophys. Res.-Atmos., 119, 4399–4412, <https://doi.org/10.1002/2013JD020482>,

1111 2014.

1112 Jaross, G.: OMPS-NPP L1G LP Radiance EV Wavelength-Altitude Grid swath orbital 3slit V2.6, Greenbelt, MD, USA,

1113 Goddard Earth Sciences Data and Information Services Center (GES DISC), Accessed: February 10, 2024,

1114 <https://doi.org/10.5067/YVE3FSNJ59RQ>, 2023.

1115 Kneizys, F. X.: Users Guide to LOWTRAN 7[M]. Air Force Geophysics Laboratory, 1988.

1116 Kramarova, N. A., Nash, E. R., Newman, P. A., Bhartia, P. K., McPeters, R. D., Rault, D. F., Sefstor, C. J., Xu, P. Q., and

1117 Labow, G. J.: Measuring the Antarctic ozone hole with the new Ozone Mapping and Profiler Suite (OMPS), Atmos.

1118 Chem. Phys., 14, 2353–2361, <https://doi.org/10.5194/acp-14-2353-2014>, 2014.

1119 Kramarova, N. A., Pawan K. Bhartia, Glen Jaross, Leslie Moy, Philippe Xu, Zhong Chen, Matthew DeLand, Lucien

1120 Froidevaux, Nathaniel Livesey, Douglas Degenstein, Adam Bourassa, Kaley A. Walker, and Patrick Sheese. Validation

1121 of ozone profile retrievals derived from the OMPS LP version 2.5 algorithm against correlative satellite measurements.

1122 Atmos. Meas. Tech., 11, 2837–2861, <https://doi.org/10.5194/amt-11-2837-2018>, 2018.

1123 Kramarova, N. A., Xu, P., Mok, J., Bhartia, P. K., Jaross, G., Moy, L., Weaver, C., Frith, S., Ziemke, J., Chen, Z., Kahn,

1124 D., Nyaku, E., Li, J., Davis, S., and Jia, Y.: Ten Year Ozone Profile Record From Suomi NPP OMPS Limb Profiler,

1125 National Oceanic and Atmospheric Administration Washington D.C., District of Columbia, United States, Technical

1126 Review NASA Peer Committee December 21, 2022.

1127 Kramarova, N. A.: OMPS-NPP L2 LP Ozone (O₃) Vertical Profile swath daily Center slit V2.6, Greenbelt, MD, USA,

1128 Goddard Earth Sciences Data and Information Services Center (GES DISC), Accessed: November, 2023,

1129 10.5067/8MO7DEDYTBH7, 2023.

1130 Kramarova, N. A., and DeLand, M.: OMPS Limb Profiler Ozone Product O₃: Version 2.6 Data Release Notes, 36pp,

1131 2023.

1132 Kramarova, N.A., Xu, P., Mok, J., Bhartia, P. K., Jaross, G., Moy, L., Chen, Z., Frith, S., DeLand, M., Kahn, D., Labow,

1133 G., Li, J., Nyaku, E., Weaver, C., Ziemke, J., Davis, S., and Jia, Y.: Decade-long Ozone Profile Record from Suomi

1134 NPP OMPS Limb Profiler: Assessment of Version 2.6 Data, Earth and Space Science, 11, e2024EA003707,

1135 <https://doi.org/10.1029/2024EA003707>, 2024.

1136 Li, F., Newman, P. A., and Waugh, D. W.: Impacts of stratospheric ozone recovery on southern ocean temperature and

带格式的: 无下划线, 字体颜色: 自动设置

域代码已更改

带格式的: 无下划线, 字体颜色: 自动设置

带格式的: 无下划线, 字体颜色: 自动设置

带格式的: 默认段落字体, 字体: (默认) +西文正文 (Calibri)

1137 heat budget, *Geophysical Research Letters*, 50(18), e2023GL103951, <https://doi.org/10.1029/2023GL103951>, 2023.

1138 Li, Z., Bi, J., Hu, Z., Ma, J., Li, B.: Regional transportation and influence of atmospheric aerosols triggered by Tonga
1139 volcanic eruption, *Environmental Pollution*, 325, 121429, <https://doi.org/10.1016/j.envpol.2023.121429>, 2023.

1140 Livesey, N. J., Read, W. G., Wagner, P. A., Froidevaux, L., Santee, M. L., Schwartz, M. J., Lambert, A., Millán Valle, L.
1141 F., Pumphrey, H. C., Manney, G. L., Fuller, R. A., Jarnot, R. F., Knosp, B. W., and Lay, R. R.: Version 5.0x Level 2 and
1142 3 data quality and description document, available at: https://mls.jpl.nasa.gov/data/v5-0_data_quality_document.pdf
1143 (last access: June 10, 2025), 2022.

1144 Llewellyn, E. J., Lloyd, N. D., Degenstein, D. A., Gattinger, R. L., Petelina, S. V., Bourassa, A. E., Wiensz, J. T., Ivanov,
1145 E. V., McDade, I. C., Solheim, B. H., McConnell, J. C., Haley, C. S., von Savigny, C., Sioris, C. E., McLinden, C. A.,
1146 Griffioen, E., Kaminski, J., Evans, W. F. J., Puckrin, E., Strong, K., Wehrle, V., Hum, R. H., Kendall, D. J. W.,
1147 Matsushita, J., Murtagh, D. P., Brohede, S., Stegman, J., Witt, G., Barnes, G., Payne, W. F., Piché L., Smith, K.,
1148 Warshaw, G., Deslauniers, D.-L., Marchand, P., Richardson, E. H., King, R. A., Wevers, I., McCreath, W., Kyrölä E.,
1149 Oikarinen, L., Leppelmeier, G. W., Auvinen, H., Mégie, G., Hauchecorne, A., Lefèvre, F., de La Noë, J., Ricaud, P.,
1150 Frisk, U., Sjöberg, F., von Schéele, F., and Nordh, L.: The OSIRIS Instrument on the Odin Spacecraft, *Canadian
1151 Journal of Physics*, 82(6), 411-422, <https://doi.org/10.1139/p04-005.2004>.

1152 Moy, L., Bhartia, P. K., Jaross, G., Loughman, R., Kramarova, N., Chen, Z., Taha, G., Chen, G., and Xu, P.: Altitude
1153 registration of limb-scattered radiation, *Atmos. Meas. Tech.*, 10, 167–178, <https://doi.org/10.5194/amt-10-167-2017>,
1154 2017.

1155 NASA: OMPS data, available at: <https://disc.gsfc.nasa.gov/datasets>, last access: February 2025a.

1156 NASA: SHADOZ data, available at: <https://tropo.gsfc.nasa.gov/shadoz/Archive.html>, last access: March 2025b.

1157 Qian, Y. Y., Luo, Y. H., Zhou, H. J., Yang, T. P., Xi, L., and Si, F. Q.: First Retrieval of Total Ozone Columns from EMI-2
1158 Using the DOAS Method, *Remote Sensing*, 16(5): 1234-1245, <https://doi.org/10.3390/rs15061665>, 2024.

1159 Rault, D. F. and Loughman, R. P.: The OMPS Limb Profiler Environmental Data Record Algorithm Theoretical Basis
1160 Document and Expected Performance, *Ieee Transactions on Geoscience and Remote Sensing*, 51(5): 2505-2527,
1161 <https://doi.org/10.1109/TGRS.2012.2213093>, 2013.

1162 **Rodgers, C. D.: *Inverse methods for atmospheric sounding: theory and practice. Vol. 2. World scientific, 2000.***

1163 Roth, C. Z., Degenstein, D. A., Bourassa, A. E., and Llewellyn, E. J.: The retrieval of vertical profiles of the ozone
1164 number density using Chappuis band absorption information and a multiplicative algebraic reconstruction technique,
1165 *Canadian Journal of Physics*, 85(11), 1225-1243, <https://doi.org/10.1139/p07-130>, 2007.

1166 Rozanov, V. V., Dinter, T., Rozanov, A. V., Wolanin, A., Bracher, A., and Burrows J.P.: Radiative transfer modeling
1167 through terrestrial atmosphere and ocean accounting for inelastic processes: Software package SCIATRAN. *Journal of
1168 Quantitative Spectroscopy & Radiative Transfer*, 194, 65-85, <https://doi.org/10.1016/j.jqsrt.2017.03.009>, 2017.

1169 Schwartz, M., Froidevaux, L., Livesey, N., and Read, W.: MLS/Aura Level 2 Ozone (O3) Mixing Ratio V005, Greenbelt,
1170 MD, USA, Goddard Earth Sciences Data and Information Services Center (GES DISC), Accessed: June 10, 2025,
1171 <https://doi.org/10.5067/Aura/MLS/DATA2516>, 2020.

1172 Thompson, A. M., Witte, J. C., Smit, H. G., Oltmans, S. J., Johnson, B. J., Kirchhoff, V. W., and Schmidlin, F. J.: Southern
1173 Hemisphere Additional Ozonesondes (SHADOZ) 1998–2004 tropical ozone climatology: 3. Instrumentation,
1174 station-to-station variability, and evaluation with simulated flight profiles, *J. Geophys. Res.-Atmos.*, 112,
1175 <https://doi.org/10.1029/2005JD007042>, 2007.

1176 University of Saskatchewan: OSIRIS data. available at: <https://research-groups.usask.ca/osiris/data-products.php>, last
1177 access: July 25, 2025.

1178 Veeffkind, J. P., de Haan, J. R., Brinksma, E. J., Kroon, M., and Levelt, P. F.: Total ozone from the Ozone Monitoring
1179 Instrument (OMI) using the DOAS technique, *Ieee Transactions on Geoscience and Remote Sensing*, 44(5):
1180 1239-1244, <https://doi.org/10.1109/TGRS.2006.871204>, 2006.

1181 [von Clarmann, T., Degenstein, D. A., Livesey, N. J., Bender, S., Braverman, A., Butz, A., Compernelle, S., Damadeo, R.,](#)
1182 [Dueck, S., Eriksson, P., et al.: Overview: Estimating and reporting uncertainties in remotely sensed atmospheric](#)
1183 [composition and temperature. Atmospheric Measurement Techniques, 13\(8\), 4393-4436, 2020.](#)
1184 Waters, J.W., Froidevaux, L., Harwood, R. S., Jarnot, R. F., Pickett, H. M., and Read, W. G.: The Earth Observing System
1185 Microwave Limb Sounder (EOS MLS) on the Aura satellite, Ieee Transactions on Geoscience and Remote Sensing,
1186 44(5), 1075-1092, <https://doi.org/10.1109/TGRS.2006.873771>, 2006.
1187 Xu, P. Q., Bhartia, P. K., Jaross, G. R., DeLand, M. T., Larsen, J. C., Fleig, A., Kahn, D., Zhu, T., Chen, Z., Gorkavyi, N.,
1188 Warner, J., Linda, M., Chen, H. G., Kowitt, M., Haken, M., and Hall, P.: Release 2 data products from the Ozone
1189 Mapping and Profiling Suite (OMPS) Limb Profiler, Proc. SPIE 9242, Remote Sensing of Clouds and the Atmosphere
1190 XIX, and Optics in Atmospheric Propagation and Adaptive Systems XVII, 92420K (17 October 2014),
1191 <https://doi.org/10.1117/12.2067320>, 2014.
1192 Young, P. J., Harper, A. B., Huntingford, C., Paul, N. D., Morgenstern, O., Newman, P. A., Oman, L. D., Madronich, S.,
1193 and Garcia, R. R.: The Montreal Protocol protects the terrestrial carbon sink, Nature 596, 384–388,
1194 <https://doi.org/10.1038/s41586-021-03737-3>, 2021.
1195 [Zawada, D. J., Rieger, L. A., Bourassa, A. E., and Degenstein, D. A.: Tomographic retrievals of ozone with the OMPS](#)
1196 [Limb Profiler: algorithm description and preliminary results. Atmos. Meas. Tech., 11, 2375–2393,](#)
1197 <https://doi.org/10.5194/amt-11-2375-2018>, 2018.
1198 Zhu, F., Li, S.W., Yang, T. P., and Si, F. Q.: Research on Inversion and Application of Ozone Profile Based on OMPS
1199 Limb Scattering Observation, Acta Optica Sinica, 45(6), 82-92, <https://doi.org/10.3788/AOS202141.0401005>, 2025.
1200 Zhu, F., Si, F. Q., Zhan, K., Dou, K., and Zhou, H. J.: Inversion of Ozone Profile of Limb Radiation in Chappuis-Wulf
1201 Band. Acta Optica Sinica, 41(4), 39-48, <https://doi.org/10.3788/AOS241244>, 2021.
1202 Zhu F., Si, F. Q., Zhou, H. J., Dou, K., Zhao, M. J., and Zhang, Q.: Sensitivity Analysis of Ozone Profiles Retrieved from
1203 SCIAMACHY Limb Radiance Based on the Weighted Multiplicative Algebraic Reconstruction Technique, Remote
1204 Sensing, 14(16), 3954, <https://doi.org/10.3390/rs14163954>, 2022.

带格式的： 缩进： 左侧： 0 厘米，
悬挂缩进： 1 字符， 首行缩进： -1
字符

删除的内容： .

-
-
-
-
-
-
-